Research Paper

Generalised and automated method for surface analysis of roughness and subsurface porosity using micro-computed tomography

Lukas Englert [*], Volker Schulze, Stefan Dietrich

Karlsruhe Institute of Technology, Institute for Applied Materials (IAM-WK), Engelbert-Arnold-Straße 4, 76131 Karlsruhe, Germany

ARTICLE INFO

ABSTRACT

As additive manufacturing enables the production of intricate, high-value parts with functional integration, inspection is gaining importance to ensure safety for use. Since the surface quality of laser beam powder bed fusion parts has proven to be inherently inhomogeneous, the measured values are dependent on the measurement spot, making surface quality difficult to characterise using conventional methods. Combined with the fact that the complex shape of the parts potentially complicates measurements further, a new surface characterisation method is required to adequately capture the quality of additively manufactured parts on the entire surface. In this work, a novel method is proposed that is both capable of meeting the above requirements and additionally allows the correlation of the results with the process data and the evaluation of the near-surface porosity. At the same time, the local quality deviations can be visualised and roughness hotspots found and correlated with the process.

1. Introduction

In the past years, additive manufacturing (AM) of complex metallic parts through laser beam powder bed fusion (PBF-LB, common synonymous acronyms are SLM or LPBF) has been more and more adopted by science and industry. The parts exhibit excellent mechanical properties and are nearly fully dense. What remains as a challenge, is the inhomogeneous distribution of defects and the relatively rough surface of the parts manufactured [1,2].

Measuring the surface topography of a part provides data $z(u,v)$ of the surface height at the coordinates u and v. To characterise the surface, various descriptive values can be calculated from this function, such as the arithmetic mean height $S_a = \frac{1}{A} \iint_A |z(u,v)| \, du \, dv$ with the area A. The height of the deepest valley is described by $S_v = |\min_A(z(u,v))|$, while the value of the highest peak is $S_p = \max_A(z(u,v))$. The sum of the largest peak height and valley depth values is $S_z = S_v + S_p$. Similar descriptors calculated for 1D data are denoted by $P_{a/v/p/z}$.

Different mechanisms, like the occurrence of the Plateau–Rayleigh instability, adhering powder or open porosity determine the generated as-built surface roughness [2,3]. To understand the interplay between these mechanisms, Whip et al. studied the effect of PBF-LB process parameters on various surface roughness parameters [4]. The authors found singular features such as surface protrusions to influence the surface roughness parameters and make the measurements ultimately influenced by measurement position. The authors concluded that the

likelihood of sampling these features needs to be statistically reflected in the measurements, and a guarantee to find the features can only be given through a measurement of the complete surface. Fox and Pintar measured a $40\,\text{mm} \times 40\,\text{mm}$ surface using focus variation microscopy and showed that a Gumbel distribution can be used to describe the S_v distribution [5]. The statistical analysis finally yielded the possibility to estimate the maximum value of S_v on a specimen from a relatively small measurement set. Nevertheless, the approach was only possible on homogeneous surfaces and thus could only provide estimates for non-systematic effects of roughness variation. Similar results regarding the inhomogeneity of AM surfaces were also observed by Sun et al. and Evans and Gockel [6,7]. As Gockel et al. and Yadollahi et al. found the maximum valley depth (S_v respectively R_v) parameter to be important for fatigue life, this seems to be of great importance as parameters like S_v, S_p and S_z are extreme values and thus largely influenced by measurement sampling [8,9]. A review on the effect of surface roughness in PBF-LB on fatigue performance by Sanaei and Fatemi also stated surface roughness to be the governing factor for fatigue performance, with the maximum valley depth being proposed to best describe the critical features of the surface [10]. In addition, area measurements were considered to be advantageous over profile measurements due to the larger measurement area. Therefore, for a reliable assessment of the performance of components with an inhomogeneous surface, the surface should be characterised if not on the entire part then at least for the highly loaded zones during application.

---

* Corresponding author.
  E-mail address: lukas.englert@kit.edu (L. Englert).

The most promising method for characterising high quality AM parts is X-ray computed tomography (XCT), as it facilitates finding the killer defect in a part [11], while offering the possibility to inspect complex parts with inaccessible internal features [12]. The identification of the most critical defects is more relevant than general density characteristics, since one large defect is more important for mechanical behaviour than uniformly distributed small pores. Recently, characterisation of the surface of AM components using XCT has also become the subject of scientific research, as the surfaces are often difficult to reach using conventional methods [10,13,14]. Moreover, XCT testing offers the possibility to investigate several key features such as defects, distortion and the surface within one method and therefore allows for a straightforward correlation of these properties. To facilitate XCT roughness measurements, several approaches have been proposed in literature. Kerckhofs et al. extracted line profiles from XCT images and compared the corresponding P_a values to conventionally measured values from optical and contact stylus profilometry [15]. For rough surfaces, the method delivered precise results and allowed inspection of lattice structures. A similar approach for cylindrical specimens was employed for extracting surface profiles by 'unrolling' the surface [16, 17]. A software to help in lattice analysis by providing functions for detection of the strut axis and extraction of surface topography was published by Oosterbeek and Jeffers [18], whereas a simplified approach was proposed by the group of du Plessis et al. [19,20]. The authors evaluated surface roughness through XCT by fitting a plane to a manually selected region of interest and subsequently calculating the deviations from this plane as roughness. A comparison to tactile measurements showed the XCT measurement to yield lower S_a values. This was explained with differences in sampling steps and the area selection. The handling of re-entrant features was not explained in detail in the method, which could also explain part of these differences. Townsend et al. extracted areal surface topography from XCT by using the surface determination algorithm offered by commercial software, converting the data to a mesh format and removing non-visible surfaces to create a height map [21]. Comparison between this method and focus variation (FV) showed that AM surfaces can be correctly characterised through this method. Using similar approaches, different researchers compared XCT surface topography measurements with traditional areal surface characterisation methods, like FV, confocal microscopy (CM) or coherence scanning interferometry (CSI), and mainly noted that the resolution of XCT is generally lower, which limits applicability to sufficiently rough surfaces in relation to the resolution of the measurement system [22–24]. On the other hand, some points, e.g. at steep flanks of the topography, were difficult to characterise in optical instruments. Additionally, the XCT measurement was able to characterise sub-surface features like open- or closed porosity and re-entrant features and is not limited by line-of-sight or a maximum slope [23]. An alternative approach to XCT surface characterisation was proposed by Pagani et al. in which re-entrant feature characterisation was accomplished by redefining the roughness parameters on a surface mesh using a parametric representation of the surface as a reference base [25]. The downside of the approach was the incompatibility with traditional measurements and standards.

Fox et al. presented XCT measurements of 2D surface topographies where the height at each point was defined as the upmost point of transition from material to air [23]. This way, a well-defined surface was obtained. By defining the first material to air transition point beneath the surface as another surface, a partial subsurface mapping of regions with defects below the surface could be obtained. However, no roughness or other numerical values were presented as a method for quantification and the methodology could not be extended to more complicated parts or arbitrary surfaces.

This work presents a new approach to the characterisation of surface and subsurface features. The novelty of the approach lies in the full automation of the XCT surface evaluation for arbitrary part geometries, allowing a comprehensive, localised and reproducible measurement of

topography and near-surface defects in complex free-form parts. In addition, the approach creates a mapping of the measured data to the input CAD geometry mesh, which facilitates the analysis of AM surfaces and could be synchronised with the slicing process and build conditions. This is particularly important, since the inhomogeneous nature of AM parts requires an analysis which characterises the entire surface and at the same time delivers a description of local roughness and defect concentrations. This way, surface parameters can be correlated to data from the build process like up- and downskin zones or possible remelting candidate areas. In future research this will enable an understanding of the origins of inhomogeneities and ultimately lead to improved compensation strategies by feedback of the local surface state correlations to the slicing and therefore build process.

2. Material and methods

2.1. Additive manufacturing

Specimens were manufactured using an ORLAS Creator machine from OR Laser GmbH which comprises a 250 W Yb fibre laser. The process was carried out without platform heating, under Argon inert gas atmosphere, 40 μm laser spot diameter, 225 W laser power and 30 μm layer height. Specimens were scanned using a core–shell strategy, with the core filled with rectilinear hatching rotated 67° between layers. The shell was fabricated with one perimeter line for even numbered layers and two perimeter lines for odd numbered layers. An offset of 90 μm was set between perimeter and hatching. Distance between scan lines was set to 150 μm while scan speed was set to 1000 mm s^{-1}. The same parameters were used for hatching and perimeter lines. To avoid a seam effect on the contour of the parts, the start and stop points of the perimeter lines were placed randomly. Gas atomised AlSi10Mg powder from m4p material solutions GmbH with a D50 of 35.3 μm and a bulk density of 1.50 g cm^{-3} was used. The chemical composition is shown in Table 1.

2.2. XCT image acquisition

XCT images were recorded on an YXLON Precision μCT using an acceleration voltage of 165 kV and a target current of 0.06 mA. For each reconstruction 2100 projections were recorded over a 360° rotation on a Perkin Elmer XRD1620 AN flat panel detector with 2048 × 2048 pixels and a pixel pitch of 0.2 mm. To reduce noise in the projection images, three measurements were recorded with an exposure time of 800 ms and averaged for each image. Image reconstruction was carried out using VGStudio MAX 3.3 with the FDK-algorithm and Shepp-Logan filtering. The reconstructed images had a resolution of 10.9 μm. The images were cut to the region containing the object by a surface determination and the pores were segmented using VGEasyPore to obtain a uniform grey value of surrounding air and porosity. This approach is nonetheless optional and not required for the method since segmentation of the image is included in the self developed image analysis algorithm.

2.3. Specimen geometries

In order to demonstrate the surface characterisation using the new method, two different specimen geometries were fabricated. The first geometry consists of a cuboid geometry that also contains a freeform surface and an undercut. The geometry mesh from CAD and a 3D rendering of the XCT scan are shown in Figs. 1(a) and 1(b). This geometry is used to explain the selection of measurement parameters, to demonstrate the ability of the method to characterise freeform surfaces, and to analyse statistics obtained from a simple specimen. The second, more complex geometry, is shown in Figs. 1(c) and 1(d). It consists of several geometric elements and overhanging structures. This geometry is used to demonstrate a detailed analysis of the surface of the tapered bore element using the novel method.

Table 1
Chemical composition of m4p AlSi10Mg powder.

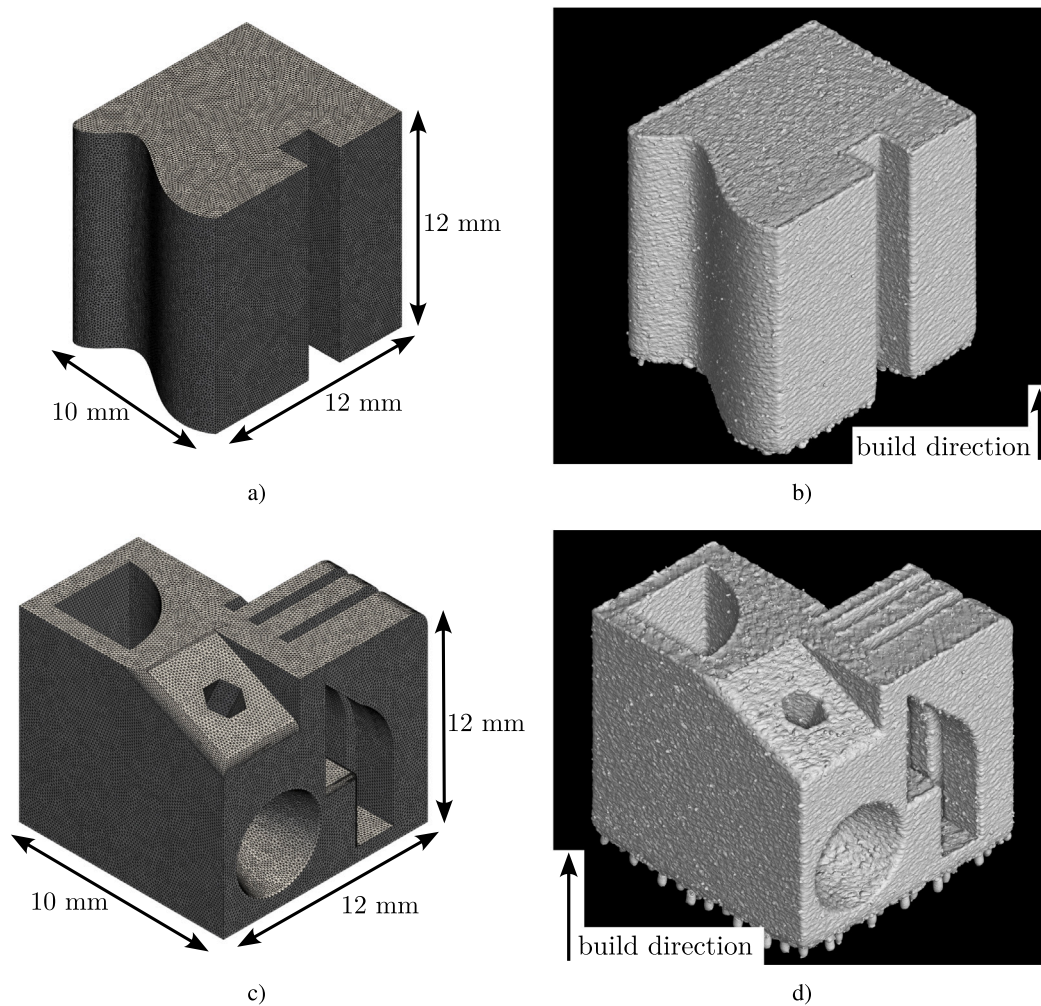|	Al	Fe	Si	Mg	Mn	Ti	Zn	Cu	Pb	Sn	Ni
Composition in wt. %	Base	0.14	9.8	0.31	< 0.01	0.01	0.01	< 0.01	< 0.01	< 0.01	< 0.01

Fig. 1. 1(a): CAD mesh of cuboid geometry. 1(b): 3D rendering of XCT scan of cuboid geometry. 1(c): CAD mesh of complex geometry. 1(d): 3D rendering of XCT scan of complex geometry.

To obtain a uniform sampling of the surface, the CAD geometry meshes of the specimen geometries were remeshed using isotropic explicit remeshing in MeshLab with a target length of $150\,\mu m$ [26]. By adjusting the target length, the density of measurement sampling can be controlled.

3. Surface analysis method

In short, the proposed method aims to measure the surface height profile in measurement windows placed around each triangle of a CAD geometry mesh from an XCT image and to calculate the roughness parameters for these windows. The information provided by the CAD geometry mesh is used to determine the measurement direction in the XCT image and to remove the shape from the measurement. Furthermore, the near-surface porosity is measured and descriptive parameters are calculated for each measurement window location. The calculated parameters can either be visualised on the input mesh or statistically analysed via a .csv output file.

The proposed analysis method is implemented in C++ using open source libraries such as Insight Toolkit (ITK), the Computational Geometry Algorithms Library (CGAL) and boost [27–29]. The first part of

the proposed method is shown as a flowchart in Fig. 2. The purpose of this method is to find a measurement spot around each triangle of the part mesh. This is achieved by selecting a pivot triangle and finding neighbouring triangles based on two conditions: The triangle vertices are within a user-defined distance to the pivot triangle midpoint and have a small angular deviation to the pivot triangle normal. A bounding box is then found around this group of triangles by applying the CGAL bykat convex hull algorithm followed by the CGAL rotating caliper algorithm [30–33]. The main axis of the bounding box, together with the averaged normal of the triangle group and the cross product of these two vectors, defines the new orientation system in which the volume image will later be resliced. Finally, the origin of the bounding box in image coordinates is needed to fully define the measurement point.

The second part of the algorithm is shown in Fig. 3. The image and CAD geometry mesh are read in using the functions provided by ITK [27]. As a preparatory step, the XCT data is registered to the spatial position of the part geometry. For this purpose, the rotational alignment is carried out in VGStudio in advance. Translational alignment is found in Paraview and used as algorithm input. A binary mask representing the air surrounding the object is generated from the input image. This is
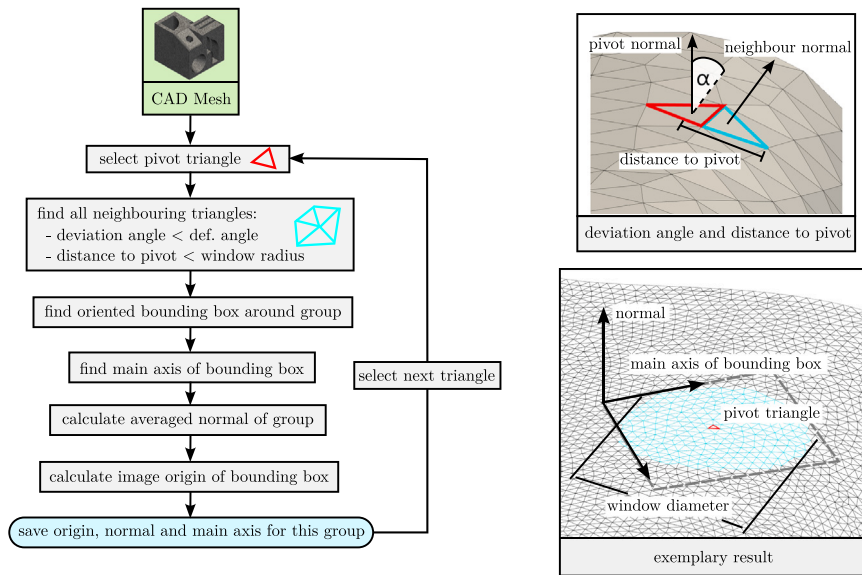
Fig. 2. Flowchart of triangle grouping algorithm with sketch of deviation angle and distance to pivot measurement and exemplary resulting grouped faces (light blue) around pivot triangle (red). (For interpretation of the references to colour in this figure legend, the reader is referred to the web version of this article.)
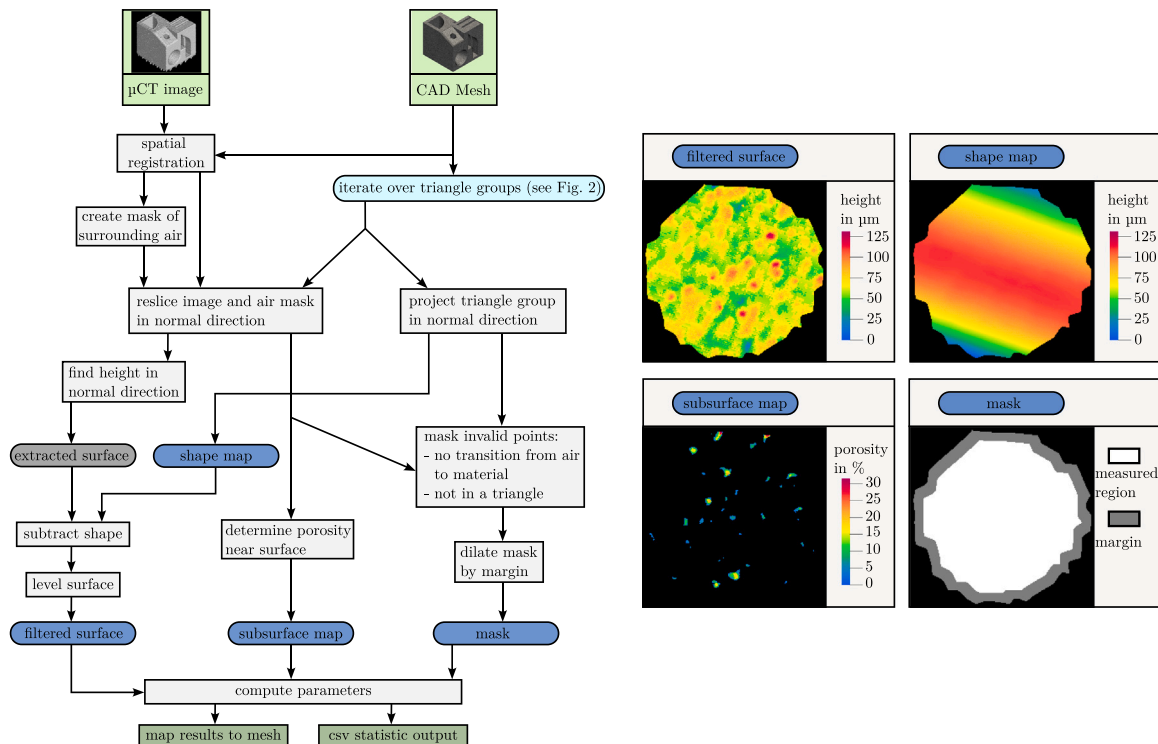

Fig. 3. Flowchart of roughness and subsurface porosity measurement algorithm. Exemplary results for the filtered surface and corresponding subsurface map as well as the shape and mask used for this example region are shown on the right side. (For interpretation of the references to colour in this figure legend, the reader is referred to the web version of this article.)

achieved by segmenting the image into material and air and labelling all connected air pixels. To separate surrounding air from pores, the label object with the highest number of pixels on the image border is selected as the surrounding air mask. The following steps are performed for each group of triangles found using the method presented in Fig. 2. First, both the input image and the surrounding air image are resliced along the normal direction of the triangle group. Using the window size, normal, and main axis found in the first part of the algorithm (cf. Fig. 2), only a small portion of the XCT dataset has to be resliced for computational efficiency. This operation causes the surface to be oriented in the slice direction in the resliced images. The reslice of the

surrounding air image is used to check if a transition from material to air can be detected in the normal direction. In this way, image regions that do not contain the object are excluded from the analysis. An additional check is performed by projecting the triangles of the group in the normal direction. Pixel coordinates that do not lie within one of the projected triangles are also excluded from the analysis. The mask of invalid pixels generated in this way can also be dilated by a margin to also exclude pixels near the window boundary. Next, a raw surface is extracted from the resliced image. This is done by finding the uppermost z coordinate containing material for each x and y position in the resliced image. This way, the measurement is made
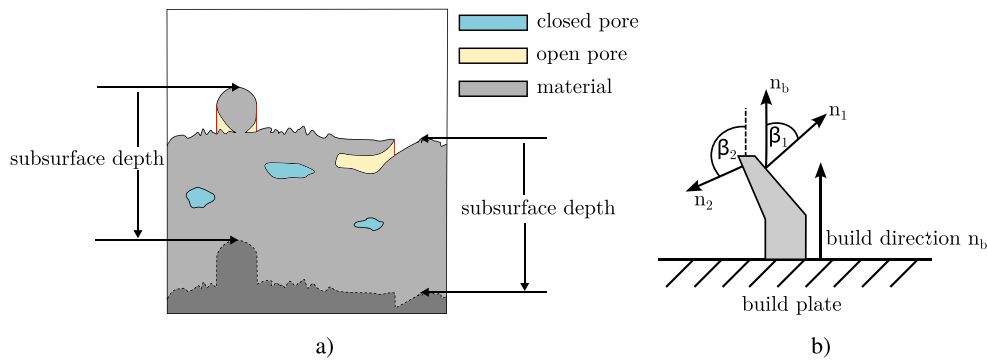
Fig. 4. 4(a): Sketch of resliced image stack and definition of measured subsurface porosity. Porosity is counted within a defined subsurface depth range measured from the surface. 4(b): Sketch of build angle determination. (For interpretation of the references to colour in this figure legend, the reader is referred to the web version of this article.)
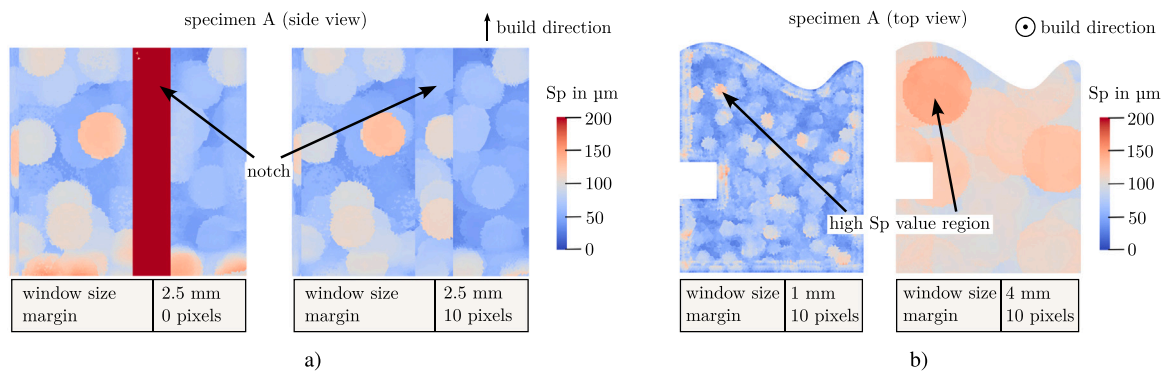

Fig. 5. S_p value mapping on specimen A with different measurement parameters. 5(a): Variation of margin parameter. 5(b): Variation of window size parameter. (For interpretation of the references to colour in this figure legend, the reader is referred to the web version of this article.)

as comparable as possible to classical optical measurement methods. The subsequent step is to remove the nominal shape of the surface from the roughness measurement. To achieve this, the triangles are projected in the normal direction. From this projection, the surface profile of the triangles is measured and a shape map is calculated. This shape map is then subtracted from the raw surface to remove the part shape from the measurement. Next, a plane is fitted to the resulting surface using a least-squares algorithm [34]. This plane is then subtracted from the surface to correct for slight misalignment during registration. The resulting filtered surface is used to calculate height parameters (S_a,S_q,S_{ku},S_{sk},S_p,S_v,S_z) according to [35]. The calculation is performed using multi-precision floats to avoid rounding errors [36]. Examples for the mask, shape and filtered surface are visualised on the right side of Fig. 3. The added margin at the boundary of the mask is shown in grey. Increasing the margin parameter shrinks the analysed window area to exclude more pixels at the window boundary.

In addition, a subsurface porosity map is generated from the projected image by counting the pore voxels at each x and y position down to a user-specified subsurface depth from the surface height. The quotient of defect voxels and total voxels provides a localised porosity measure. This process is shown schematically in Fig. 4(a). It is also possible to distinguish between open and closed porosity by using the surrounding air mask. Due to the definition of subsurface porosity used here, open porosity can result from re-entrant features, e.g. underneath spatter particles (left in the sketch) or open pores (right in the sketch). Different features, like volumetric porosity, maximum and average projected pore size for open, closed and total porosity are finally calculated through functions provided by ITK from the subsurface porosity map [37].

The calculated height parameters, together with the subsurface porosity parameters, are written to a .csv output file for analysis and also mapped to the input geometry mesh in .vtk file format. This .vtk file can be rendered in Paraview to visualise the spatial distribution

of the calculated features [38]. Additionally, as shown in Fig. 4(b), a build angle β_i is determined for each triangle of the input geometry. The build angle is calculated between the build direction n_b (perpendicular to the build plate) and the normal of each triangle n_i. By correlating the height parameters with the build angle values, the results can be analysed separately by build angle.

A compiled executable binary and the source code of the implementation are available under https://github.com/IAM-WK/CT4AM_Surface.

4. Results on example specimens

4.1. Measurement parameter selection

Similar to conventional optical measurement methods, several measurement parameters need to be set. The important parameters are the subsurface depth, the window size, and a measurement margin. The subsurface depth is chosen depending on what is considered 'near-surface' in a particular case. In this work, it was set to the average width of three scan tracks ($450\,\mu m$) in order to capture pores located in the interface region between perimeter and hatching. The window size and measurement margin are selected on the basis of a small preliminary study presented in this section. The measurement margin is the value in pixels by which the mask is dilated to exclude any measurements at the boundary region.

Fig. 5(a) shows the side view of the S_p value mapping on the cuboid geometry with different margin parameters. The left image shows the measurement results with no measurement margin and the right image shows the results with the same window size and a margin of 10 pixels. It is visible, that the S_p values inside the notch are very high compared to the rest of the specimen with no measurement margin. In comparison, plausible values are obtained with a margin of 10 pixels. The reason for this behaviour is that peaks on the side surface of the
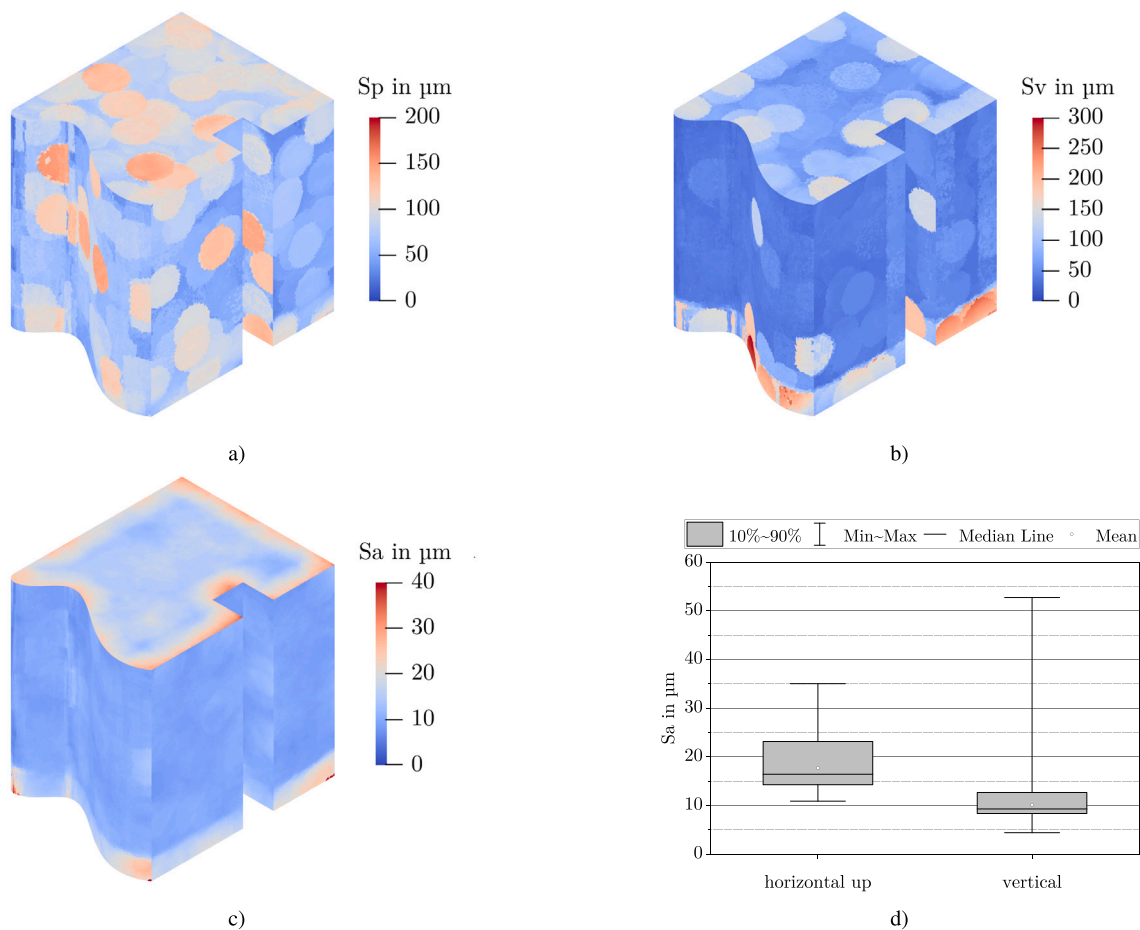
Fig. 6. Roughness mapping of 6(a): S_p value, 6(b): S_v value and 6(c): S_a value. 6(d): S_a value statistics on sides and horizontal upskin. (For interpretation of the references to colour in this figure legend, the reader is referred to the web version of this article.)

notch are visible in the projection images for the notch surface and are recognised as peaks. Since these values only occur at the boundaries of the measurement region, they can be avoided by selecting a suitable margin value. In summary, the margin should be high enough to avoid specimen boundary effects, but also small enough to sample as much of the specimen surface as possible.

The left image in Fig. 5(b) shows the top surface S_p value mapping on the cuboid geometry with a window size of 1 mm compared to the window size of 4 mm in the right image. The higher value results in larger regions being assigned higher S_p values. The S_p value corresponds to the highest peak in a measurement window and is therefore governed by spatter particles on the surface of the specimens. Larger measurement windows result in the inclusion of spatter in more distant triangle locations. In conclusion, larger measurement windows result in more stable features, but make it difficult to find localised surface variations. In contrast, small window sizes are prone to measurement noise and may not be representative of a specimen surface spot. In the following, the window size was set to 2.5 mm and the measurement margin to 10 pixels.

4.2. Cuboid geometry

Next, an analysis of the cuboid geometry is presented to demonstrate the capability of the method to provide localised analysis on flat as well as free-form surfaces. Fig. 6 shows colour field visualisations of different height parameters mapped to their measurement locations. Figs. 6(a) and 6(b) show the maximum peak height and maximum valley depth distribution. Locations with high values are apparently randomly distributed throughout the specimen in the shape of circles.

These locations correspond to singular features that determine these extreme value surface parameters, such as spatter particles in the case of the S_p value. The circular shape is caused by the circular analysis window which contains the critical surface feature within a certain radius. The S_v value is visibly influenced by the bottom edge of the specimen. As visible in the XCT image in Fig. 1(b), the high values at the base are caused by instabilities in the process when building the first few layers above the support structures. Other than that, regions with a high S_v value are rather sparsely distributed compared to regions with a high S_p value.

The average arithmetic roughness S_a is shown in Fig. 6(c). It is visible that S_a is particularly high at the base of the specimen and at the rim of the horizontal upskin. The high values at the base are caused by the same mechanisms as for the S_v parameter. The higher values at the rim of the horizontal upskin are caused by bulging of the perimeter. Fig. 6(d) shows a box plot of the values measured on the horizontal upskin and the vertical sides. It is evident that the majority of the values measured on the vertical side show only a small spread around the mean value, although the maximum measured value is more than five times higher than the mean value. The range of values in the horizontal upskin is smaller (around 11 μm to 35 μm). In contrast, the band from 10 % to 90 % of measured values is wider than on the vertical sides, covering a variance of about 9 μm in comparison to about 4 μm on the vertical side.

4.3. Complex geometry

Overview. Fig. 7 shows the mapping of the analysis results to the geometry mesh of the complex geometry, demonstrating the feasibility of analysing undercut and inaccessible geometries that cannot
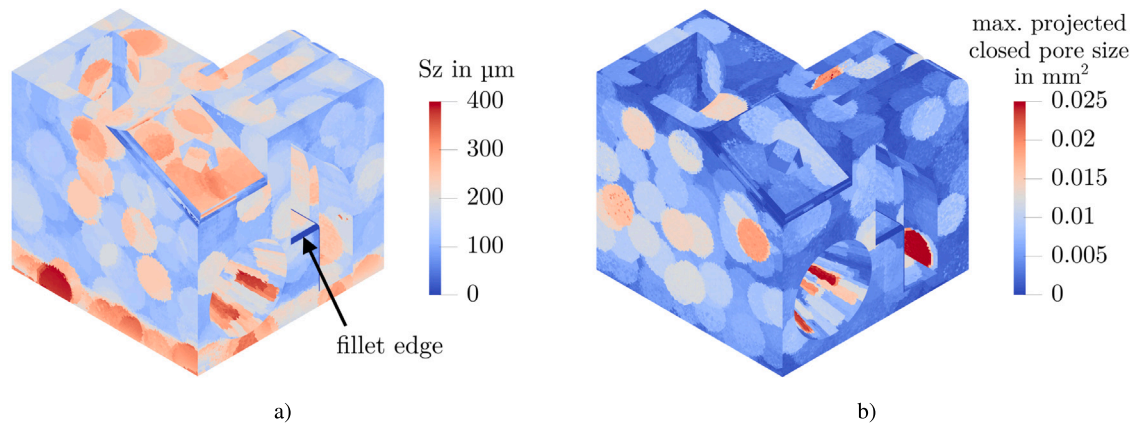
Fig. 7. Complex geometry analysis results: 7(a): S_z mapping, 7(b): Maximum projected size of closed pores mapping. (For interpretation of the references to colour in this figure legend, the reader is referred to the web version of this article.)

be 'unrolled' like cylindrical surfaces. Some triangles were assigned a value of 0, which is due to the fact that the measurement algorithm marked the windows at these locations as invalid due to their size. This minimum window size requirement was introduced, as a minimum measurement pixel count is needed to ensure a valid plane could be fitted to the measurement data. The minimum required size depends on the roughness of the part, as high roughness amplitudes lead to unstable least squares plane fitting. The small measurement windows are created at locations where the deviation to the neighbouring triangles is too high to find large enough contiguous windows. These locations are highly curved areas, which mainly correspond to fillet edges.

Fig. 7(a) shows the mapping of the S_z value to the complex geometry. It can be seen that the base edge exhibits high S_z values, similar to the S_v value mapping on the cuboid geometry. In addition, the inclined upskin surface at the top of the specimen shows elevated S_z values. Fig. 7(b) shows the mapping of the maximum projected size of closed pores, i.e. the largest projected near-surface pore in each measurement window, on the complex geometry mesh. It is visible that, similar to the results of the roughness analysis, this feature is inhomogeneously distributed. There is no apparent concentration of high values, instead the extremal values are seemingly randomly distributed over the surface of the specimen.

Analysis of taper bore. The surface of the mantle of the taper bore is now analysed in depth. Fig. 8(a) shows a front view of the XCT image of the taper bore region. It is visible, that the surface quality is best at the regions which are oriented perpendicular to the build direction and worst at the upper region which is built as an unsupported overhanging region. Also, the lower region of the bore exhibits a larger amount of spatter particles and adhering powder compared to the side surface. A side view of a cut 3D rendering of the XCT image is shown in Fig. 8(b). The cut plane shows the material below the bore mantle surface with pores visible as dark regions. The depth which is considered as near-surface is visualised as a dashed line. The subsurface region of the example cut plane contains open pores, re-entrant features and closed porosity.

The visual impression of the surface quality is confirmed by the S_a mapping in Fig. 8(c). As a visual aid, the build angle (calculated from the normal vector relative to the build direction) is denoted at three locations. At the lowest point of the bore, the build angle is 20° relative to the build direction, while the top point of the bore is build at an angle of 160° relative to the build direction. The S_a value shows a clear dependence of the build angle, with the overhanging surface having the worst surface quality with S_a values up to 40 µm and the lower region of the bore showing roughness hotspots corresponding to the regions with most adhering spatter. In contrast, the S_a values on the side surface are between around 8 µm to 18 µm, which can still be considered a high variation only based on measurement location.

Fig. 8(d) shows the spatial distribution of the volumetric open porosity distribution in the mantle surface of the taper bore. Especially the downskin regions contain open porosity, but also some spots in the low-build angle region which mainly correspond to regions with a high amount of spatter particles. The side-by-side comparison with the S_a mapping reveals some correlation between the hotspots, although not every high value in the S_a mapping corresponds to high open porosity values at the same location.

A quantitative analysis is carried out by classifying the roughness and subsurface porosity values by the build angle in 10° classes and plotting the resulting distributions in Figs. 8(e) and 8(f). For the arithmetic mean roughness S_a it is visible, that the roughness is minimal at 90° build angle, while lower as well as higher build angles lead to increased roughness. Besides the increased mean value of roughness, also the variation of measured roughness values is minimal at 90° build angle and increases with lower and higher build angles. Similarly, for the volumetric open porosity measurements plotted in Fig. 8(f) the mean value and variation is minimal in the 100° build angle class. Here, the values at lower build angles are also higher than at 90° or 100° build angle, but the values at the downskin build angles are considerably higher than at the low build angles. The correlation of the distribution of the two values is mainly caused by the high values having similar causes. Adhering spatter and unstable build conditions in the downskin region lead to high roughness and at the same time to surface protrusions and open pores.

5. Discussion

5.1. Automated XCT roughness measurement

The accuracy of XCT roughness measurements compared to conventional techniques has already been discussed elsewhere and was generally found to be accurate when the resolution of the XCT measurement was high enough to capture the most important features of a surface, which, for example, include spatter particles or open pores [21,24]. However, the exact procedure for extracting the surface profile differed between studies. Since the exact implementation of XCT measurement procedures affects the measurement results, standardisation of XCT roughness measurement methods is needed for future development. For example, researchers followed different approaches to extract the height profile data from the image. In some studies, the surface was converted to a mesh, while in others the data at each pixel location was used directly after segmentation. Re-entrant features were also treated with different approaches.

In existing work, areal measurements were mainly defined by manually registering a surface to match the Z-plane in the XCT image and manually selecting a region of interest from this image. Compared to
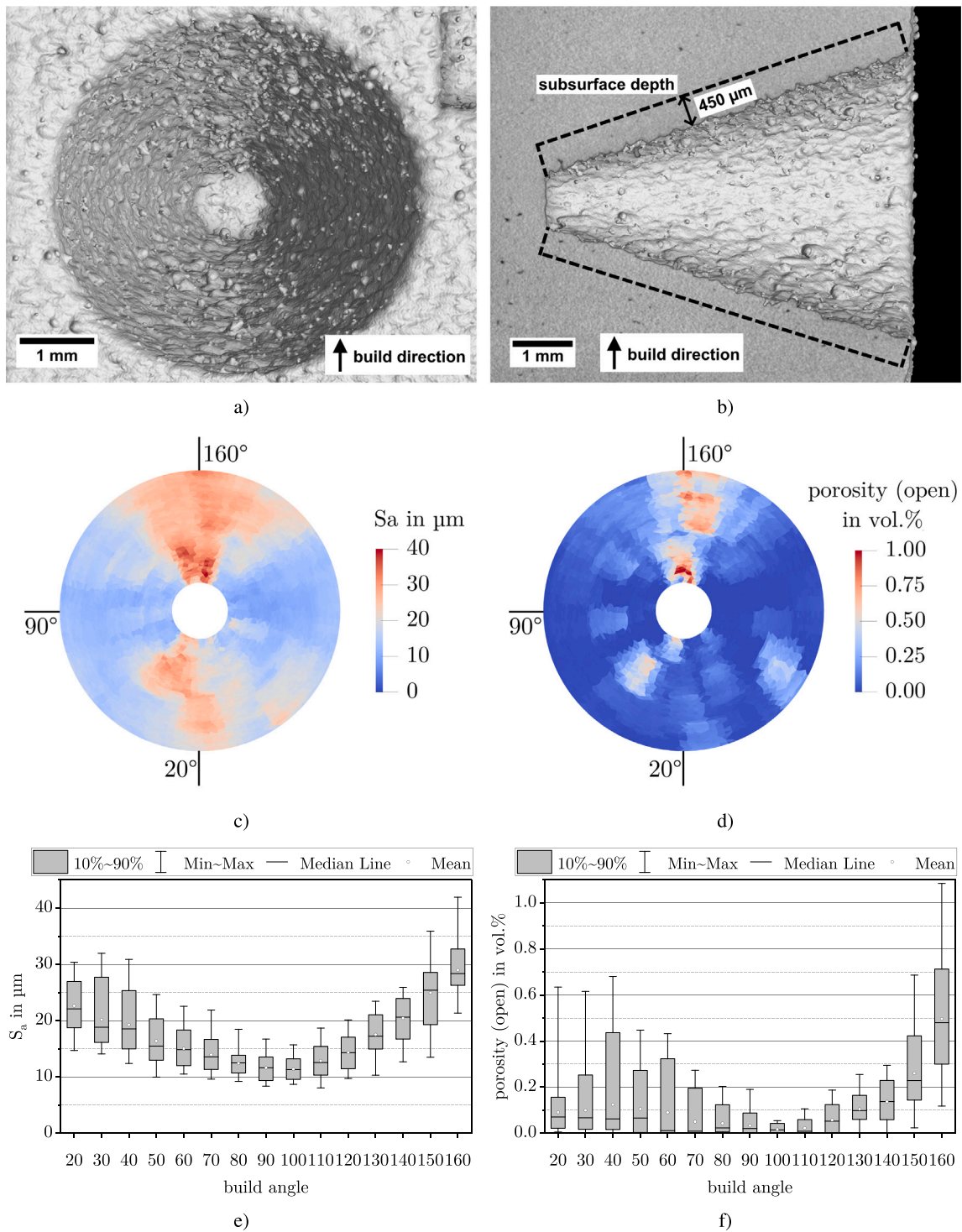
Fig. 8. Evaluation of taper bore geometry: 8(a): Front view 3D rendering of XCT image of taper bore geometry, 8(b): Side view of cut 3D rendering of XCT image of taper bore geometry, 8(c): Visualisation of spatial distribution of S_a value, 8(d): Visualisation of spatial distribution of volumetric open porosity value, 8(e): Distribution of S_a value in dependence of build angle, 8(f): Distribution of volumetric open porosity value in dependence of build angle. (For interpretation of the references to colour in this figure legend, the reader is referred to the web version of this article.)

the proposed method, which uses information from the geometry mesh for this step, this approach is not reproducible. The proposed method includes a clear definition of how to define the surface measurement direction and how to set up the projection window for measurement. Defining the reference normal from the CAD mesh is limited in its applicability to highly distorted parts, but offers the advantage of associating and correlating the information obtained with the CAD mesh.

Automating the definition of the measurement direction not only provides reproducible measurements, but also allows for localised analysis that would otherwise be far too time-consuming. By associating each result value array with a mesh triangle, an easy-to-understand visualisation of the results is achieved. Statistical analysis can be applied to obtain information about the range of roughness values on AM parts and to find critical values that may occur only once on a part's surface. Moreover, the direct connection of results to mesh data enables

automated evaluation with respect to the build angle. When comparing the findings on the build angle dependency of surface roughness and open porosity/re-entrant features of the present work with the work of Fritsch et al. [17], a few differences in the findings are noticeable. Fritsch et al. found that surface roughness was only dependent on the build angle in the downskin region, while the present work also found a dependence in the upskin region (see Fig. 8). Fritsch et al. also found the amount of re-entrant features to be linearly correlated with the profile surface roughness P_a. While comparability is limited due to different roughness metrics and different re-entrant feature definitions, this relationship could not be found in the present work. The inconsistency in the results could also be due to variations between specimens built with different machines and settings or the specimen geometry, so further research is needed to collect larger data sets to understand these relationships.

In the implemented version, the algorithm took about 90 min for the analysis of geometry A on an Intel i9 12900 processor, using about 6 GB of RAM. However, further optimised implementations may allow faster analysis.

When comparing XCT roughness measurement with tactile or optical methods, it is evident that, in addition to the aforementioned advantages, disadvantages also exist. The part size that can be analysed is limited by the thickness that can be penetrated by X-rays. In addition, the resolution achievable on large components may be too low to reproduce the surface topography with sufficient accuracy. To analyse these components, multiple scans may need to be combined, or the component could be cut to smaller pieces before scanning.

5.2. Shape removal

In the proposed method the shape is removed by subtracting the projected height profile of the mesh geometry from the extracted surface. Compared to previous research in which cylindrical surfaces were evaluated by 'unrolling' the segmented surface and analysing the resulting surfaces [8,16,17], this method has some advantages and disadvantages. The disadvantage of subtracting the projected geometry is that a small geometric bias is introduced into the measured data, since the height is subtracted in the projection direction and not always perpendicular to the surface. However, the advantage of this approach is that it works for all geometries, not just cylindrical or other surfaces with zero Gaussian curvature. In addition, there is no need to find a centroid where deviations can lead to artificial unevenness of a surface, as is the case with the 'unrolling' method.

5.3. Sampling the 'right' spot

An important issue in assessing the surface quality of additively manufactured parts is how representative data can be obtained for a specimen. Conventionally machined surfaces show less variation in surface quality across the surface, so this problem, although fundamental in nature, has only recently arisen in AM [5,7]. The approach of statistical modelling of the roughness on the surface of a specimen by Fox and Pintar [5] is only applicable if the sampled data is not spatially correlated and there is no systematic variation in roughness between different regions of a part's surface. To increase the confidence in the estimated S_v value, the sampled surface area also has to be increased, which ultimately leads to long measurement times. In addition, only an estimate of the extreme value can be obtained, not the location where that extreme value occurs.

Compared to the existing work on this topic, which focuses on finding the minimum area that can be considered representative for a specimen, the presented method follows a different approach of analysing the entire specimen to guarantee finding the maximum values. By analysing the entire surface of a specimen, the mean and maximum values of the roughness parameters are obtained, while the spatial location of roughness and defect hotspots can be determined.

These hotspots are caused by the AM process and make it difficult to find a representative measurement spot in conventional measurement procedures.

As shown in Figs. 6 and 7, the measured parameters do not only vary randomly over the surface of a specimen, but there exist regions with systematically different roughness values. When measuring roughness with conventional methods, i.e. on small areas, careful consideration must be given to whether the results are representative of the entire surface. The minimum area required is dependent on the variability in roughness that occurs on a specimen surface. A complete analysis of a specimen using the new method can be used as a basis for understanding the variability and spatial differences that occur. The understanding of the interrelation between geometric characteristics, such as the build angle, and the resulting distribution of surface quality metrics is needed to develop guidelines for assessment of AM surfaces. Moreover, the variability of occurring values itself can be used as a feature to evaluate the build quality of additively manufactured parts.

5.4. Near-surface porosity analysis

A similar method to analyse subsurface porosity was proposed by Fox et al. [23]. However, Fox et al. did not evaluate the resulting map of subsurface pores or propose numerical features to be extracted from the measurement. In this work, for the first time, parameters are established to evaluate subsurface porosity in the same way that roughness parameters are used to evaluate surface measurements. It is worth noting that Fox et al. used a different definition of subsurface porosity compared to the definition used in this work. Fox et al. compared the height profiles resulting from probing the surface in the XCT from either side, i.e. starting from the surrounding air vs. starting from the inside of the material, and tracking each variation as a subsurface pore. Compared to the definition proposed in the present work, this has the disadvantage, that closed pores cannot be distinguished from open features such as open pores and undercuts. Furthermore, only the size of pores perpendicular to the normal direction can be evaluated and not the length of pores in normal direction.

The comprehensive analysis of specimens in terms of surface quality and subsurface porosity could be used to correlate these features to improve the understanding of common causes of defects. A similar investigation was conducted by the group of Yonehara et al. [39]. Yonehara et al. [39] found correlations between porosity and some roughness parameters, although the density and surface quality were only treated as global parameters for different parameter sets. A localised analysis using the novel method could improve insight into the mechanisms governing both surface quality and porosity.

The evaluation of near-surface porosity is also of interest in the assessment of parts which are subjected to oscillating loads and are therefore susceptible to fatigue failure. As Sanaei and Fatemi pointed out, near-surface defects are particularly critical to fatigue performance and, together with surface roughness, near-surface defects have a synergistic effect on fatigue life [40]. Since the novel method is capable of analysing both subsurface porosity and surface quality, it could be used in future work to gain a deeper understanding of which defect or combination of defects controls component failure predominantly. Finally, these insights could be used to further improve the surface parameters recently proposed by Lee et al. [41] or Gu et al. [42] for evaluating fatigue-critical additively manufactured parts. The localised evaluation of surface and subsurface quality of a part would then allow for an estimate of failure critical regions.

6. Conclusion

In the present work, a novel method was proposed for the automated evaluation of roughness and near-surface porosity from XCT scans of additively manufactured freeform parts. Two exemplary specimens were analysed to demonstrate the capabilities of the new method.

- The novel method allows analysis of the entire surface of a specimen, facilitating the determination of mean and extreme values of various roughness parameters for statistical evaluation.
- The visualisation of the spatial distribution of the roughness parameters makes it possible to locate function-critical regions.
- Geometry and build process parameters can be correlated with roughness metrics to gain insight into process-structure–property relationships.
- Correlations between near-surface porosity and surface roughness can be evaluated automatically to improve understanding of the PBF-LB process.
- The surface of a part is analysed in a local context, with shape removal being based on the geometry of the CAD mesh. In this way, freeform surfaces can be analysed using the novel method.

For future work, it is planned to use the data collected using the method for selective post-processing of additively manufactured surfaces. To this end, a robot-controlled surface finishing will be applied only to critical surfaces identified by XCT.

CRediT authorship contribution statement

Lukas Englert: Conceptualization, Data curation, Investigation, Software, Writing – original draft. **Volker Schulze:** Supervision, Writing – review & editing. **Stefan Dietrich:** Funding acquisition, Project administration, Writing – review & editing.

Declaration of competing interest

The authors declare that they have no known competing financial interests or personal relationships that could have appeared to influence the work reported in this paper.

Data availability

Data will be made available on request.

Acknowledgements

References

[1] Wang S, Ning J, Zhu L, Yang Z, Yan W, Dun Y, et al. Role of porosity defects in metal 3D printing: Formation mechanisms, impacts on properties and mitigation strategies. Mater Today 2022. http://dx.doi.org/10.1016/j.mattod.2022.08.014.

[2] Cabanettes F, Joubert A, Chardon G, Dumas V, Rech J, Grosjean C, et al. Topography of as built surfaces generated in metal additive manufacturing: A multi scale analysis from form to roughness. Precis Eng 2018;52:249–65.

[3] Masiagutova E, Cabanettes F, Sova A, Cici M, Bidron G, Bertrand P. Side surface topography generation during laser powder bed fusion of AlSi10Mg. Addit Manuf 2021;47:102230.

[4] Whip B, Sheridan L, Gockel J. The effect of primary processing parameters on surface roughness in laser powder bed additive manufacturing. Int J Adv Manuf Technol 2019;103(9):4411–22.

[5] Fox JC, Pintar AL. Prediction of extreme value areal parameters in laser powder bed fusion of nickel superalloy 625. Surf Topogr Metrol Prop 2021;9(2):025033.

[6] Sun W, Giusca C, Lou S, Yang X, Chen X, Fry T, et al. Establishment of X-ray computed tomography traceability for additively manufactured surface texture evaluation. Addit Manuf 2022;50:102558.

[7] Evans R, Gockel J. Surface roughness variation in laser powder bed fusion additive manufacturing. In: 2021 international solid freeform fabrication symposium. University of Texas at Austin; 2021, p. 458–66.

[8] Gockel J, Sheridan L, Koerper B, Whip B. The influence of additive manufacturing processing parameters on surface roughness and fatigue life. Int J Fatigue 2019;124:380–8.

[9] Yadollahi A, Mahtabi M, Khalili A, Doude H, Newman J. Fatigue life prediction of additively manufactured material: Effects of surface roughness, defect size, and shape. Fatigue Fract Eng Mater Struct 2018;41(7):1602–14.

[10] Sanaei N, Fatemi A. Defects in additive manufactured metals and their effect on fatigue performance: A state-of-the-art review. Prog Mater Sci 2021;117:100724.

[11] du Plessis A, Beretta S. Killer notches: The effect of as-built surface roughness on fatigue failure in AlSi10Mg produced by laser powder bed fusion. Addit Manuf 2020;35:101424.

[12] Waller JM, Parker BH, Hodges KL, Burke ER, Walker JL. Nondestructive evaluation of additive manufacturing state-of-the-discipline report. Technical Report, National Aeronautics and Space Administration; 2014.

[13] Townsend A, Senin N, Blunt L, Leach R, Taylor J. Surface texture metrology for metal additive manufacturing: A review. Precis Eng 2016;46:34–47.

[14] Leach RK, Bourell D, Carmignato S, Donmez A, Senin N, Dewulf W. Geometrical metrology for metal additive manufacturing. CIRP Ann 2019;68(2):677–700.

[15] Kerckhofs G, Pyka G, Moesen M, Van Bael S, Schrooten J, Wevers M. High-resolution microfocus X-ray computed tomography for 3D surface roughness measurements of additive manufactured porous materials. Adv Energy Mater 2013;15(3):153–8.

[16] Persenot T, Burr A, Dendievel R, Buffière J-Y, Maire E, Lachambre J, et al. Fatigue performances of chemically etched thin struts built by selective electron beam melting: Experiments and predictions. Materialia 2020;9:100589.

[17] Fritsch T, Farahbod-Sternahl L, Serrano-Munoz I, Léonard F, Haberland C, Bruno G. 3D computed tomography quantifies the dependence of bulk porosity, surface roughness, and re-entrant features on build angle in additively manufactured IN625 lattice struts. Adv Energy Mater 2022;24(6):2100689.

[18] Oosterbeek RN, Jeffers JR. StrutSurf: A tool for analysis of strut morphology and surface roughness in additively manufactured lattices. SoftwareX 2022;18:101043.

[19] du Plessis A, Sperling P, Beerlink A, Kruger O, Tshabalala L, Hoosain S, et al. Standard method for microct-based additive manufacturing quality control 3: Surface roughness. MethodsX 2018;5:1111–6.

[20] du Plessis A, Tshibalangananda M, Yadroitsava I, Yadroitsev I. On the evaluation of surface roughness: X-ray tomography reveals hidden details. In: progress in additive manufacturing 2020. 2020, p. 208–22. http://dx.doi.org/10.1520/STP163720200094.

[21] Townsend A, Racasan R, Leach R, Senin N, Thompson A, Ramsey A, et al. An interlaboratory comparison of X-ray computed tomography measurement for texture and dimensional characterisation of additively manufactured parts. Addit Manuf 2018;23:422–32.

[22] Lou S, Zhu Z, Zeng W, Majewski C, Scott P, Jiang X. Material ratio curve of 3D surface topography of additively manufactured parts: An attempt to characterise open surface pores. Surf Topogr Metrol Prop 2021;9(1):015029.

[23] Fox JC, Kim F, Reese Z, Evans C, Taylor JS. Investigation of complementary use of optical metrology and x-ray computed tomography for surface finish in laser powder bed fusion additive manufacturing. In: ASPE conference: Dimensional accuracy and surface finish in additive manufacturing. 2017, p. 132–6.

[24] Thompson A, Senin N, Giusca C, Leach R. Topography of selectively laser melted surfaces: A comparison of different measurement methods. CIRP Ann 2017;66(1):543–6.

[25] Pagani L, Townsend A, Zeng W, Lou S, Blunt L, Jiang XQ, et al. Towards a new definition of areal surface texture parameters on freeform surface: Re-entrant features and functional parameters. Measurement 2019;141:442–59.

[26] Hoppe H, DeRose T, Duchamp T, McDonald J, Stuetzle W. Mesh optimization. In: Proceedings of the 20th annual conference on computer graphics and interactive techniques. 1993, p. 19–26.

[27] McCormick M, Liu X, Jomier J, Marion C, Ibanez L. ITK: Enabling reproducible research and open science. Front Neuroinform 2014;8. http://dx.doi.org/10.3389/fninf.2014.00013.

[28] The CGAL Project. CGAL user and reference manual. 5.5.1 ed.. CGAL Editorial Board; 2022, URL https://doc.cgal.org/5.5.1/Manual/packages.html.

[29] Boost. Boost C++ libraries. 2023, https://www.boost.org/. [Last accessed 24 April 2023].

[30] Hert S, Schirra S. 2D convex hulls and extreme points. In: CGAL user and reference manual. 5.5.1 ed.. CGAL Editorial Board; 2022, URL https://doc.cgal.org/5.5.1/Manual/packages.html#PkgConvexHull2.

[31] Bykat A. Convex hull of a finite set of points in two dimensions. Inform Process Lett 1978;7(6):296–8.

[32] Fischer K, Gärtner B, Herrmann T, Hoffmann M, Schönherr S. Bounding volumes. In: CGAL user and reference manual. 5.5.1 ed.. CGAL Editorial Board; 2022, URL https://doc.cgal.org/5.5.1/Manual/packages.html#PkgBoundingVolumes.

[33] Toussaint GT. Solving geometric problems with the rotating calipers. In: Proc. IEEE melecon, volume 83. 1983, p. A10.

[34] Alliez P, Pion S, Gupta A. Principal component analysis. In: CGAL user and reference manual. 5.5.1 ed.. CGAL Editorial Board; 2022, URL https://doc.cgal.org/5.5.1/Manual/packages.html#PkgPrincipalComponentAnalysisD.

[35] DIN EN ISO 25178-2:2012. Geometrical product specifications (GPS) surface texture: Areal Part 2: Terms, definitions and surface texture parameters. Beuth Verlag GmbH; 2012.

[36] Hemmer M, Hert S, Pion S, Schirra S. Number types. In: CGAL user and reference manual. 5.5.1 ed.. CGAL Editorial Board; 2022, URL https://doc.cgal.org/5.5.1/Manual/packages.html#PkgNumberTypes.

[37] Lehmann G. Label object representation and manipulation with ITK. Insight J 2007;8(1):31.

[38] Squillacote AH, Ahrens J, Law C, Geveci B, Moreland K, King B. The paraview guide, volume 366. Kitware Clifton Park, NY; 2007.

[39] Yonehara M, Kato C, Ikeshoji T-T, Takeshita K, Kyogoku H. Correlation between surface texture and internal defects in laser powder-bed fusion additive manufacturing. Sci Rep 2021;11(1):1–10.

[40] Sanaei N, Fatemi A. Analysis of the effect of surface roughness on fatigue performance of powder bed fusion additive manufactured metals. Theor Appl Fract Mech 2020;108:102638.

[41] Lee S, Rasoolian B, Silva DF, Pegues JW, Shamsaei N. Surface roughness parameter and modeling for fatigue behavior of additive manufactured parts: A non-destructive data-driven approach. Addit Manuf 2021;46:102094.

[42] Gu H, Jiao L, Yan P, Guo Z, Qiu T, Wang X. A surface skewness and kurtosis integrated stress concentration factor model. J Tribol 2023;145(4):041702. http://dx.doi.org/10.1115/1.4056455.